Materials Advances

ROYAL SOCIETY OF CHEMISTRY

PAPER

View Article Online
View Journal | View Issue

Cite this: *Mater. Adv.*, 2025, **6**, 9179

Degradation of CV dye by the as-synthesized Fe^0–TiO_2 supported clinoptilolite under UV and solar irradiations

Nazia Aziz,[a] Hamida Panezai,*[a] Jihong Sun,[b] Noor Samad Shah,[c] Raza Ullah,[d] Ruohan Xu[b] and Zakira Jogezai[a]

Textile industries release toxic organic dyes into wastewater, harming aquatic ecosystems and affecting photosynthesis. This study aims to synthesize a photocatalyst for the efficient degradation of crystal violet (CV) dye in aqueous media. Titanium dioxide (TiO_2) is the most preferable photo-catalyst, but its fast electron–hole recombination rate and low adsorption capacity have limited its applications on a large scale. To enhance the adsorption and degradation efficiency, a TiO_2-supported clinoptilolite (CP) and a porous composite of zerovalent iron (Fe^0) co-doped with titanium dioxide/clinoptilolite (Fe^0–TiO_2/CP) were synthesized using sol–gel and borohydride reduction methods, respectively. The effects of various parameters like acidity, temperature and concentration on the photo-catalytic activity, morphological and micro-structural features and surface areas of different TiO_2/CP and Fe^0–TiO_2/CP composites were characterized by various techniques such as X-ray diffraction (XRD), Scanning electron microscopy (SEM), energy dispersive X-ray analysis (EDXA), Fourier transform infrared (FTIR) spectroscopy, UV-Visible spectroscopy, thermogravimetric (TG) and differential thermogravimetric (DTG) analyses and Brunauer–Emmett–Teller (BET) isotherm. The as-synthesized composites (TiO_2/CP and Fe^0–TiO_2/CP) were used as photocatalysts to remove CV dye from water. The parent CP and TiO_2 achieved 51% and 58% removal efficiency of CV dye under UV radiation, respectively. The 0.25 M TiO_2/CP composite showed the highest degradation efficiency (92.3%) under UV radiation, while 0.1 M TiO_2/CP performed best under solar radiation (88.5% removal) in 120 minutes. Theoretical analysis *via* kinetic models revealed that the adsorption and degradation processes of CV dye followed pseudo-second-order (PSO) and pseudo-first-order (PFO) kinetic models, respectively. The TiO_2/CP composite mainly produces hydroxyl radicals ($^{\bullet}OH$) during dye degradation, while Fe^0–TiO_2/CP generates both $^{\bullet}OH$ and superoxide radicals ($^{\bullet}O_2^-$). This $^{\bullet}O_2-$ radical enhances the degradation efficiency of Fe^0–TiO_2/CP due to Fe^0's favorable reduction potential. CV mineralization occurs through two pathways: *N*-demethylation and hydroxyl radical attack on the central carbon, leading to degradation and complete mineralization. Moreover, the structure, morphology and particle size of the composite play vital roles in the extent of their photocatalytic efficiencies. Therefore, a combination of compositional and structural engineering of TiO_2-based photocatalysts is expected to give better device performance. However, further investigation is needed in the near future.

Received 20th June 2025,
Accepted 14th October 2025

DOI: 10.1039/d5ma00658a

rsc.li/materials-advances

1. Introduction

Water scarcity is the most serious challenge of today's growing world. The usage and disposal of different biological and chemical effluents in water bodies cause rapid quality degradation of water and chronically deplete the water resources.[1] Various non-pretreated dyes from the textile industries are continuously getting released into the water, endangering it to the point where it is unsafe for consumption and putting the population's health at risk.[2] CV dye is important in the artificial coloration of textile materials on a large scale. It is a water-

[a] *Department of Chemistry, Faculty of Basic Sciences, Balochistan University of Information Technology, Engineering and Management Sciences, Quetta, 87300, Pakistan. E-mail: hameeda.panezai@buitms.edu.pk, panezaihamida@yahoo.com*
[b] *Beijing Key Laboratory for Green Catalysis and Separation, Department of Chemistry and Chemical Engineering, Beijing University of Technology, Beijing, 100124, PR China*
[c] *Department of Chemistry, COMSATS University Islamabad, Abbottabad-Campus, KPK 22060, Pakistan*
[d] *College of Mechanical Engineering, Shandong University of Technology, Shandong 255000, China*

soluble and non-biodegradable dye, and its improper discharge into water bodies has raised a major environmental concern.[3] By using various eco-friendly methods, wastewater containing dyes is efficiently treated. In this study, the combination of adsorption and heterogeneous photo-catalysis is employed for the degradation of CV dye under dark and light-assisted UV and solar irradiations.[4] The key photocatalyst responsible for the degradation is the semiconductor TiO_2.[5–7] TiO_2 exhibits a number of drawbacks, including limited reaction efficiency under solar radiations, difficulty in the catalyst recovery steps, limited surface area that results in poor adsorption capacity, a large bandgap and fast rate of electron–hole recombination, which in turn limited its practical application as a photocatalyst on large scale.[5–7]

To enhance the photo-catalytic and adsorption efficiency of TiO_2, several strategies are employed, such as morphology controlling,[8] elemental doping,[9] surface loading[7,10] and energy band engineering.[11,12] Among these strategies, the most promising is the loading of TiO_2 onto the surface of nanoporous adsorbents and elemental doping with TiO_2 to overcome the drawbacks of TiO_2 efficiency.[7] Clinoptilolite is an effective supporting adsorbent for TiO_2 due to its characteristics, such as porosity (34%), excellent resistance to extreme temperatures, ion-exchange capacity (2.16 meq g^{-1}) and bulk density (1.15 g cm^{-3}).[5,6,13]

The energy difference between the valence band (VB) and conduction band (CB) of TiO_2 is in the UV radiation region, so the radiation absorption capability in the visible region is still relatively low. Using solar light as an energy source is less effective in the TiO_2 photocatalytic process because the composition of UV light in the sun is only 5–7%.[14] Thus, modification of the TiO_2 photocatalyst is required in order to absorb light in the solar light region. To expand the photocatalyst response into the visible spectrum, an iron metal-doped TiO_2 (Fe^0–TiO_2) composite was found to be an effective photocatalyst for dye degradation when exposed to UV and visible light.[15]

In the present study, different molar TiO_2/CP composites were prepared using the sol–gel method. The second type of composites used for the degradation of CV dye was Fe^0–TiO_2 and Fe^0–TiO_2/CP, which were synthesized using a simple borohydride reduction method. The adsorption rate and photocatalytic degradation efficiency of CV dye from aqueous solution by various molar composites of TiO_2/CP, Fe^0–TiO_2 and Fe^0–TiO_2/CP and the role of active free radicals, such as OH, $^{\bullet}O_2^-$ and h^+, in CV dye degradation were studied using a UV-visible spectrophotometer. The effects of various parameters, like temperature, concentration on photo-catalytic activity, micro-structural feature, surface area, pore size, pore volume, crystal phase and photo-catalytic capacity of TiO_2/CP, Fe^0–TiO_2 and Fe^0–TiO_2/CP composites, were characterized using X-ray diffraction (XRD), scanning electron microscopy (SEM), energy dispersive X-ray analysis (EDXA), Brunauer–Emmett–Teller isotherm (BET), and Fourier transform infrared (FTIR) spectroscopy and thermogravimetric (TG) and differential thermogravimetric (DTG) analyses. The adsorption and degradation kinetic processes of CV dye were theoretically analyzed using pseudo-first-order and pseudo-second-order models, respectively. The degradation pathway of CV dye was studied using heated electrospray ionization (H-ESI) coupled with a mass spectrometer.

2. Experimental section

2.1. Materials

Clinoptilolite was supplied by VSK ProZeo Zeolite, Slovakia. CV dye of high purity, $FeSO_4{\cdot}7H_2O$ and sodium borohydride (98%) were purchased from Sigma Aldrich. $TiCl_4$ was purchased from Fluka, and ammonia (32%) and HCl (37%) were purchased from Merck Schuchardt, Germany.

2.2. Synthesis and post-synthesis

TiO_2 and different molar ratio composites of TiO_2/CP were synthesized using the sol gel method, as reported by Ullah *et al.* in 2021.[7] In order to synthesize the Fe^0/TiO_2 composite, a 30 mL solution was synthesized by mixing ethanol and water (5 : 25 v/v), and 0.800 g of already synthesized TiO_2 was added to the mixture with continuous stirring. Then, 1.200 g of $FeSO_4{\cdot}7H_2O$ was added to the TiO_2 solution and stirred for 30 minutes under vacuum. After that, a 40 mL solution of sodium borohydride (1.200 g) was prepared in deionized water and added dropwise to the TiO_2 solution under an inert atmosphere with continuous stirring to achieve maximum reduction. With the addition of the first drop of $NaBH_4$, a black precipitate of Fe^0/TiO_2 was formed. The black precipitates were separated after complete reduction, washed with ethanol and then vacuum dried at 60 °C. The sample was ground and stored at room temperature in an air-tight container to protect the composite powder from oxidation by air. The Fe^0–TiO_2/CP was also prepared using the method mentioned above with already synthesized 0.1 M TiO_2/CP (0.800 g) powder.

2.3. Adsorption and photo-catalytic activity of the composites

The removal of CV dye through adsorption and photocatalytic degradation was conducted at room temperature in duplicate. A 100 mL solution of 10 ppm CV dye was prepared in a 250 mL beaker. Then, 3 mL of the solution was extracted for zero/standard reading. Afterwards, 50 mg of photocatalyst was added, and the mixture was stirred for 30 minutes at 140 rpm in the dark using a hot plate and magnetic stirrer to achieve adsorption/desorption equilibrium. Moreover, during the adsorption process, a 3 mL sample was withdrawn from the suspension at a specific time interval (10, 20 and 30 minutes). In order to study the dye degradation, the same solution was then placed under UV radiation, and 3 mL sample was withdrawn at a particular time interval (10, 20, 40, 60, 90 and 120 minutes). After irradiation, the withdrawn samples were centrifuged at 3000 rpm for 8 minutes to remove suspended particles of the composite from the solution.

The light source used was a UV lamp (0.02 mW cm^{-2}) enclosed in a rectangular wooden box. A UV-Vis spectrophotometer (PerkinElmer, Lambda 25) was used to analyze the absorbance of CV dye concentration at λ_{max} (585 nm). The same dye degradation procedure that was previously performed

under a UV source was employed using solar radiation in a photochemical reactor. The percentage removal efficiency and the adsorbed quantity of dye per unit mass (mg g^{-1}) of adsorbent at equilibrium were calculated using the following equations:

$$\text{Removal}\% = \frac{(C_0 - C_t)}{C_0} \times 100 \quad (1)$$

$$\text{Adsorption capacity}(q_t) = C_0 - C_t \times \frac{\text{Vol of soln in Liter}}{\text{Mass of adsorbent in grams}} \quad (2)$$

where C_0 and C_t are the concentrations (mol L^{-1}) of CV dye at the initial stage (t = 0) and at time t (minutes), respectively.

2.4. Degradation pathway study of CV dye

Two 5 mL samples were withdrawn at two time intervals (20 and 120 minutes) after irradiation during the photocatalytic activity experiment. The withdrawn samples were centrifuged at 3000 rpm for 8 minutes to remove the suspended particles of the composite from the solution. The analysis of the CV dye degradation pathways was performed using a triple quadrupole mass spectrometer, model TSQ Quantis (Thermo Electron Scientific, USA), equipped with a heated electrospray ionization (H-ESI) source. The instrument was operated in both negative and positive ion modes, with a capillary voltage of 4.0 kV and a capillary temperature of 275 °C. Methanol was used as the solvent, and the sample was introduced using the direct insertion method at a flow rate of 10 μL min^{-1}. The sheath gas flow rate was set to 15 units, and the auxiliary gas flow rate was set to 3 units. The mass spectrometer was set to scan a mass range of 30–1500 m/z. Fragmentation (MS/MS) was performed on various peaks selected for fragmentation using collision energy ranging from 10 to 40 V. The instrument was controlled, and the data were acquired using Xcalibur software. This setup allowed for a detailed analysis of the CV dye degradation pathways, providing insights into the structures of the degradation products and the mechanisms of degradation.

2.5. Physicochemical characterization techniques

The physical and chemical properties, composition, quality, stability, and purity of the synthesized composites were examined by physicochemical characterization.[16]

The crystalline structure of CP, as-synthesized TiO_2, composites of synthesized TiO_2/CP, and Fe^0–TiO_2/CP were characterized using XRD (Bruker D8) with Cu Ka (λ = 0.1542 nm) radiation. The morphology of the samples mentioned above was studied using SEM (JEOL SEM IT200) operated at an accelerating voltage between 13.0 and 16.0 kV, and TiO_2 nanoparticles were investigated using a JEOL JEM-2100 TEM. The TG/DTG analysis was performed using a simultaneous thermal analyzer (PerkinElmer STA 8000) at a heating rate of 10 °C min^{-1} under N_2 flow in the temperature range of 0–900 °C. A JW-BK-300C surface area and micropore size analyzer (Beijing JWGB Sci and Tech Co., Ltd) were used to assess the sample's BET surface area by N_2 adsorption/desorption isotherms at 77 and 298 K. The FTIR spectrometer (Bruker ALPHA-T) was used in the wavenumber range of 4000–400 cm^{-1} to evaluate the chemical structures of the composites. The band gap of the composites was analyzed using the absorbance spectra of the samples recorded on a UV-VIS spectrometer (UV-2600, SHIMADZU).

3. Results and discussion

3.1. Structural analysis

The XRD patterns of parent CP, TiO_2 and their composites of various molarities are shown in Fig. 1. The characteristic peaks of CP, the anatase phase of TiO_2 and Fe^0 are confirmed by comparing their values with JCDPS values reported in the literature.[5] The specific peaks observed at 25.4°, 37.5°, 47.7°, 53.6°, 54.7° and 62.3° are assigned to the anatase phase of TiO_2, as shown in Fig. 1(a). The peaks present at 9.8°, 22.1°, 26.4°, 30.1° and 35.7° depicted in Fig. 1(b) are attributed to the main features of CP. Moreover, in the composites of TiO_2/CP of different molarities (Fig. 1(A)-(c)–(f)), the characteristic peaks of both TiO_2 and CP are observed, revealing that their individual crystalline structure is intact and unchanged during the composite formation. However, a decrease in the peak intensities and a slight shift of peaks of CP towards higher 2 theta angles are observed, which confirms the successful loading of TiO_2 on the surface of CP.[5] This is attributed to the fact that during the synthesis, high calcination temperature may cause dealumination and desalination, which in turn leads to a decline in peak intensity of CP. Moreover, as shown in Fig. 1(A)-(c)–(f), the characteristic peak intensity of TiO_2 at 2θ = 25.4° increases linearly with an increase in molar ratios of TiO_2 in 0.1, 0.25, 0.5 and 1.0 M TiO_2/CP composites.

In the Fe^0–TiO_2 composite, as shown in Fig. 1(B)-(g), the apparent peaks of Fe^0 at 2θ = 44° with characteristic peaks of TiO_2 are observed, which confirms the successful doping of Fe^0 with TiO_2. Two very small peaks at 2θ = 31.9° and 33.7°, as shown in Fig. 1(B)-(g), indicate the presence of iron oxide (FeO) in the sample, which is formed during the doping of Fe^0, as reported in the literature. The crystalline structure of TiO_2 was not affected by co-doping with Fe^0, which is in close agreement with a previous study conducted by Bibi *et al.*[17]

In the XRD pattern of the Fe^0–TiO_2/CP composite (Fig. 1(B)-(h)), the characteristic peaks of TiO_2 and Fe^0 are relatively less intense compared to the peaks of CP. The loading of TiO_2 and Fe^0 onto the CP framework results in a decrease in the overall peak intensities of CP, TiO_2 and Fe^0. Notably, the incorporation of Fe^0 does not significantly alter the crystalline structure of the zeolite, except for a reduction in peak intensities. This suggests that the Fe^0 particles are likely dispersed or incorporated within the CP framework without disrupting its underlying structure.[18]

The incorporation of TiO_2 into the clinoptilolite zeolite framework led to a reduction in crystallinity, resulting in decreased sharpness and intensity of the XRD peaks of CP in all molar composites. This phenomenon occurs because the introduction of TiO_2 disrupts the ordered arrangement of the zeolite's framework, causing distortions and a slight decrease

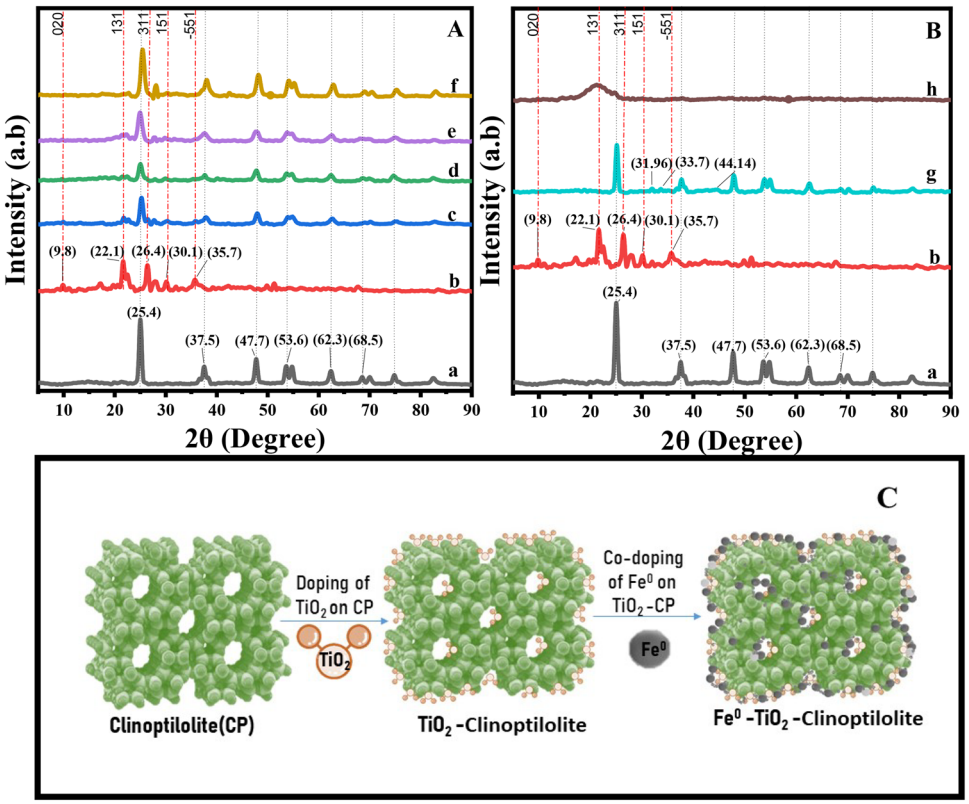

Fig. 1 XRD patterns of A: (a) TiO_2, (b) parent CP, (c) 0.1, (d) 0.25, (e) 0.5 and (f) 1.0 M TiO_2/CP and B: (g) Fe^0–TiO_2 and (h) Fe^0–TiO_2/CP. C: doping and co-doping of TiO_2 and Fe^0, respectively, on CP.

in crystallinity. As illustrated in Fig. 1(C), the surface and pores of CP become covered with TiO_2 and Fe^0 particles, leading to the formation of amorphous regions.

3.2. Morphological analysis

SEM images of CP, TiO_2, composites of TiO_2/CP and Fe^0–TiO_2/CP are shown in Fig. 2. The CP exhibited a leaf-like structure with multiple layers or sheet morphology. A pure TiO_2 particle has an irregular but somewhat spherical shape. The TiO_2 particles are deposited on the surface of CP, as clearly demonstrated by SEM images of various TiO_2/CP composites.

Although TiO_2 covers the surface of CP, it does not disrupt the structure; however, TiO_2 covers the surface of CP and the sheet-like shape of CP that are clearly seen in the SEM images of all TiO_2/CP composites and confirms the intact structure of the composites after doping.[5,7] Fe^0 particles exhibit a spherical shape and exist in chain form, which looks like spongy material.[18,19] The surface structure of CP in Fe^0–TiO_2/CP composite looks highly rough and spongy due to the doping of Fe^0, as shown in Fig. 2. Due to its spongy nature, the Fe^0 doping on the surface of TiO_2/CP composite covers the maximum area of CP zeolite. In terms of covering the maximum surface area of CP, the Fe^0 doping decreases the adsorption capacity of the Fe^0–TiO_2/CP composite due to the decreased average mesopore size of the composite, and this decreased efficiency is in good agreement with the decreased peak intensities obtained in the XRD pattern of the Fe^0–TiO_2/CP composite. Meanwhile, the EDXA spectrum of each sample shows that the main elements, such as Al, Si, and O, are spread almost throughout the CP structure, as illustrated in Fig. S1. In addition, the EDXA spectrum contains high concentrations of key elements, such as Al, Si, and O, along with metals like Na, K, Ca, and Mg, while the peaks for Ti and Fe metals confirm the successful doping of TiO_2 and Fe^0 in the CP composites.

3.3. Analysis of thermal properties

The TG and DTG curves of the composites heated in a temperature range of 0–900 °C are illustrated in Fig. 3. The TG/DTG analysis showed that CP, TiO_2 and their composites are highly stable at higher temperatures up to 900 °C, as no changes occurred in the structure of any composites. However, a very slight weight loss occurred due to dehydration of water, but no other internal structural changes were observed.[20,21] The calculated Si/Al ratio of parent CP zeolite and all of its as-synthesized composites is around 4 that has re-confirmed their thermal stability at high temperatures and found in close agreement with the literature.[21] Si/Al ratio of CP is 4.76, which is confirmed by EDXA analysis, as shown in Fig. S1.

The TGA curve of TiO_2 reveals a total weight loss of 2.5%, which can be attributed to a three-step dehydration process as evidenced by the three distinct peaks of DTG curve (Fig. 3). The first step, occurring between 46–91 and 39–226 °C in DTG and TG profiles, is characterized by a broad endothermic peak corresponds to a weight loss of 0.9%. This step is associated

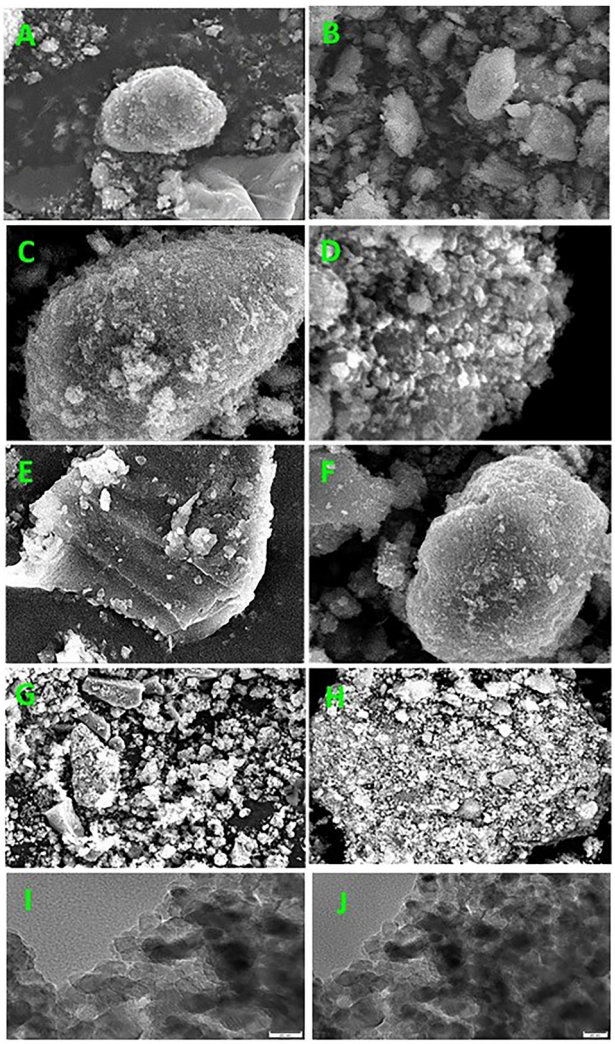

Fig. 2 SEM images of (A) TiO_2 and (B) CP. Different molar composites: (C) 0.1, (D) 0.25, (E) 0.5, and (F) 1.0 M of TiO_2/CP (G) Fe^0–TiO_2 and (H) Fe^0–TiO_2/CP, and (I) and (J) TEM of TiO_2.

with the desorption of loosely bound physisorbed water located on the external surface of TiO_2. The second step, observed between 196–273 and 226–381 °C of DTG and TG curves, exhibits a sharp endothermic peak and is linked to a weight loss of approximately 1.1%. This step is thought to be involved in the removal of tightly bound chemisorbed water from the framework structure of TiO_2. The third step, taking place over a higher temperature range of 381–900 °C of TG, is marked by a gradual weight loss of 0.5% and may be attributed to the condensation of $Ti(OH)_2$ to TiO_2 in the TiO_2 sample.[22]

In the TG curve of CP, a sharp decrease of 2.4% weight loss is observed due to the dehydration of physisorbed moisture from 40 to 225 °C, and a slow but continuous weight loss of 2.2% between 225 and 900 °C may be associated with the dehydration of water from internal cavities of the CP zeolite structure. The broad endothermic peak at 75–178 °C and a sharp endothermic peak at 224–272 °C in the DTG curve aid these two-step dehydration processes in CP zeolite.[20]

Total weight losses of about 6.0, 6.5, 6.3 and 5.6% in 0.1, 0.25, 0.5 and 1.0 M TiO_2/CP composites are calculated from the TG curves, respectively. The first steep TG curves show the loss of physisorbed water in the temperature range of 38–240 °C. The second slight TG curve shows the slow dehydration of water from the internal CP cavities in the temperature range of 240–900 °C. These two-step dehydration processes in different molar composites of TiO_2/CP are supported by the two endothermic peaks that appear in the DTG curves, as shown in Fig. 3.

The calculated weight losses of around 9.9 and 10.8% in Fe^0–TiO_2 and Fe^0–TiO_2/CP composites, respectively, are due to the evaporation of water and ethanol. A gradual and small increment in weight above 390 °C up to 760 °C is observed in both Fe^0–TiO_2 and Fe^0–TiO_2/CP composites possibly due to the formation of iron oxide at higher temperatures. This increment in the weight of Fe^0-doped composites is also confirmed by the small exothermic DTG curves, as shown in Fig. 3.

Alver *et al.* also reported that generally in all zeolites, the weight loss up to 500 °C is due to dehydration, while the slow weight loss at high temperature is due to dehydroxylation.[20] Generally, dehydroxylation is a slow process and occurs between 500 and 600 °C. At low temperatures, chemisorption took place between 28 and 41 °C on the surface of CP, as shown in Fig. 3. In the TG curves, a comparatively large peak is observed, leading to a weight gain of about 2% from 100 to 102% between 28 and 41 °C in almost all composites due to the absorption of water at low temperature. However, in Fe^0–TiO_2 and Fe^0–TiO_2/CP composites, a small peak is observed in the TG curves above 100%, indicating that the spongy structure of Fe^0 decreases the adsorption capacity of the composites, which is why water is less adsorbed compared to other composites, reconfirming the above findings in SEM and XRD.

3.4. Surface area analysis

Table 1 and Fig. S2 present the BET surface area, micro, mesopore volume and average mesopore sizes of parent CP, TiO_2, composites of TiO_2/CP and Fe^0–TiO_2/CP obtained from their N_2 adsorption/desorption isotherms measured at 77 and 298 K. All the samples were degassed under helium gas at 150 °C/423 K for 6 h prior to N_2 adsorption/desorption isotherms.

BET isotherms are used to investigate the porous structure of materials, and the form of the isotherm indicates the type of porosity in the material. The modifications made by doping of TiO_2 and Fe^0 have caused structural variations, which result in strong effects on the BET surface area, micro and mesopore volume and size in all types of TiO_2/CP composites due to the increasing molarity of TiO_2. Compared to the parent CP, the TiO_2 doped CP samples exhibit significantly increased surface area, particularly in the 0.5 M TiO_2/CP composite (76.25 $m^2\ g^{-1}$). In all the TiO_2/CP and Fe^0–TiO_2/CP composites, both the surface area and micropore volume increase compared to parent CP and pristine TiO_2, while the mesopore volume and average mesopore sizes decrease with increasing the molar ratio of TiO_2 and with the co-doping of Fe^0. These changes are attributed to

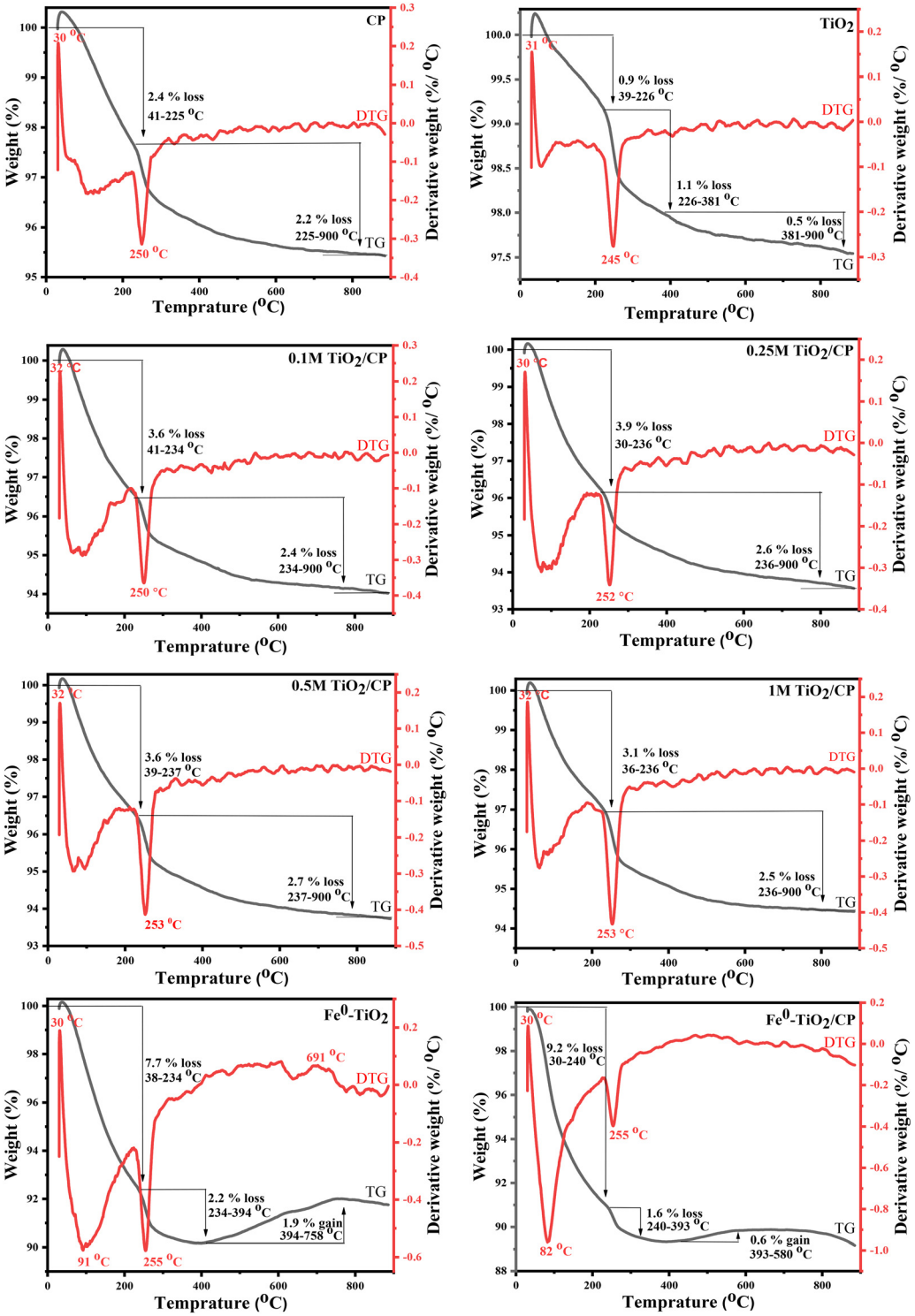

Fig. 3 TG/DTG profiles of pure CP, TiO_2, 0.1, 0.25, 0.5, 1.0 M TiO_2/CP, and Fe^0–TiO_2 and Fe^0–TiO_2/CP composites measured at a heating rate of 10 K min^{-1} under N_2 flow.

the particle size of TiO_2 (4.25 μm) and Fe^0 (0.90 μm), as reported in the literature.[18]

The particle sizes of TiO_2 and Fe^0 are very small compared to the mesopore volume and size of the parent CP, where inside the mesopore both the TiO_2 and Fe^0 are adsorbed on the surface of CP and cover the maximum surface area, which results in decreasing adsorption of CV dye and is found in close agreement with a previous study conducted by Panezai *et al.*[23]

As shown in Fig. S2, the profile for TiO_2 demonstrates a clearly defined plateau at lower relative pressures, indicating

monolayer adsorption; as pressure increases, adsorption accelerates, indicating multilayer adsorption and capillary condensation at higher relative pressures. An obvious H3 hysteresis loop in the physisorption isotherm at higher relative pressures (0.4–0.1) is observed, which is a distinguishing feature of adsorption in mesoporous materials. The H3 type hysteresis loop according to the IUPAC classification observed in these composites is common for nonporous, macroporous, and mesoporous solids.[23] This is due to differences in the gas adsorption and desorption paths within the pores.[24] A steep desorption branch and a somewhat flat adsorption branch, with a hysteresis loop that closes at high relative pressure, are frequently connected with materials containing aggregation of platelet-like particles and slit-shaped pores.

The distinct increase in adsorbate volume in the low P/P_0 region and a barely noticeable plateau, as well as an irregular shape, are observed in Type II and IV isotherms, revealing the presence of micropores associated with mesopores in the CP and its composites. An important feature is the closed hysteresis loop, with less steepness corresponding to a more uniform pore system containing capillaries with wider profile bodies and narrow, short necks. These phenomena are obviously illustrated in Table 1 and Fig. S2, where both the BET surface area and the relevant pore volume ($0 < P/P_0 < 0.1$) of all the composites, with the exception of 0.1 M TiO_2/CP are higher than parent CP (19.16 $m^2\ g^{-1}$ and 0.10 $cm^3\ g^{-1}$). This increase in both the surface area and pore volume could be attributed to increased nitrogen adsorption into TiO_2, Fe^0 and particularly on their CP support.

3.5. Optical characterization

Fig. 4 presents the FTIR spectra of CP, TiO_2 and their combined composites in the wave number range of 4000–400 cm^{-1}. The intense peak at around 1020 cm^{-1} is associated with the asymmetric stretching vibration of O–Si(Al)–O in the CP structure. As shown in Fig. 4(A)-(b), the characteristic peaks appeared at 786 and 459 cm^{-1} in CP, and their composites are attributed to stretching vibrations of AlO_4 and SiO_4 tetrahedral atoms present in zeolite structures.[7] As shown from c to f in Fig. 4(A), the peaks present in CP zeolite at 1020, 786 and 459 cm^{-1} decrease slightly due to the increasing molar ratio of TiO_2, and these peaks appear very weak in Fig. 4(A)-(g), (h) due to doping of two different materials (titania and Fe^0 metal), which is found in good agreement with the XRD patterns.

The adsorption bands at 1600 and 1560 cm^{-1} in pure TiO_2 represent the bending vibrations of Ti–OH, as shown in Fig. 4(B), and the very small absorption bands generated at 419 and 408 cm^{-1} in TiO_2 and all molar composites of TiO_2/CP are attributed to the bending vibrations of Ti–O–Ti bonds, as shown in Fig. 4(C).[18]

3.6. Bandgap analysis

In order to investigate the band gap of CP, TiO_2, TiO_2/CP and Fe^0–TiO_2/CP composites, solid UV Vis spectroscopy absorption peaks were used with the Tauc relation, as mentioned in the following equation:

$$(Ah\nu)^n = B(h\nu - E_g), \quad (3)$$

where A is absorbance, h is Planck's constant, ν is the speed of light, E_g is the band gap energy of material, B is the proportionality constant, and superscript n has a value of 2 for allowed direct transition and 1/2 for allowed indirect transition. The energy equation of quantum mechanics is as follows:

$$E = \frac{h\nu}{\lambda}, \quad (4)$$

where energy (E) represents the band gap, Planck's constant (h) is 6.626×10^{-34} Joules per second, velocity of light (ν) is 2.99×10^8 meters per second, and wavelength (λ) is the absorption peak value. The band gaps of the CP, TiO_2 and Fe^0-doped TiO_2 and TiO_2/CP composites are determined by plotting $(Ah\nu)^{1/2}$ against energy eV ($h\nu/\lambda$) for the indirect band gap and $(Ah\nu)^2$ against energy eV ($h\nu/\lambda$) for the direct band gap.[25] The linear part of the curve $(Ah\nu)^n$ against energy eV is extrapolated (Fig. S3), and the band gap energy is listed in Table 1.

In general, it is observed that rutile phase TiO_2 has less photocatalytic property compared to the anatase phase. However, anatase phase TiO_2 has a bandgap of 3.11 eV, which is best suited under UV radiation. Many studies have been conducted in order to tune and decrease the bandgap of TiO_2 and shift its efficiency towards solar radiation by various metals and non-metal co-doping.[12,18] The bandgap in TiO_2-doped CP zeolite composites decreases with the increasing surface area. It can be observed in Table 1 and Fig. S3 that the bandgap of TiO_2 decreased from 3.11 eV to 2.98 eV in the 0.1 M TiO_2/CP composite. There is a very slight decrease observed in the bandgap of 0.25, 0.5 and 1 M composites; this indicates that if the molar ratio of TiO_2 increases, then the amount (1 g) of the CP zeolite is not enough to decrease the bandgap.[26]

Table 1 BET surface area, pore volume and size and band gap of different photocatalysts

S. no	Sample	Surface area ($m^2\ g^{-1}$)	Mesopore volume ($cm^3\ g^{-1}$)	Average mesopore size (nm)	Micropore volume ($cm^3\ g^{-1}$)	Median micropore size (nm)	Direct bandgap (eV)	Indirect bandgap (eV)
1	CP	19.16	0.10	19.87	0.007	0.72	3.90	3.78
2	TiO_2	40.22	0.41	38.81	0.015	0.84	3.11	2.96
3	0.1 M TiO_2/CP	38.58	0.23	23.15	0.015	0.88	2.98	2.62
4	0.25 TiO_2/CP	53.53	0.28	19.79	0.020	0.89	3.02	2.66
5	0.5 TiO_2/CP	76.25	0.36	18.11	0.028	0.86	3.10	2.95
6	1.0 TiO_2/CP	71.61	0.39	20.58	0.028	0.88	3.01	2.91
7	Fe^0–TiO_2	55.79	0.21	14.60	0.021	0.85	1.91	1.39
8	Fe^0–TiO_2/CP	69.73	0.26	13.95	0.026	0.86	2.24	1.10

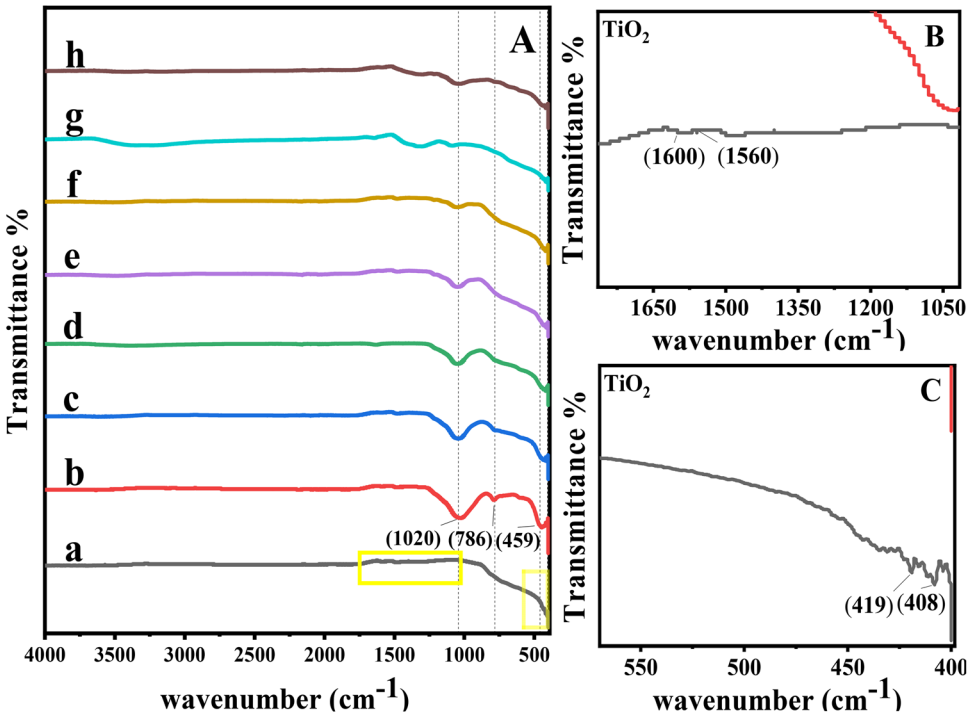

Fig. 4 FTIR spectra of A: (a) TiO_2, (b) parent CP, (c) 0.1, (d) 0.25, (e) 0.5, (f) 1.0 M TiO_2/CP, (g) Fe^0–TiO_2/CP and (h) Fe^0–TiO_2. B and C are the insets of A.

TiO_2-supported clinoptilolite (TiO_2/CP) composites can reduce TiO_2's electron–hole pair recombination rate *via* numerous mechanisms:

• Electron trap: the clinoptilolite zeolite structure can serve as an electron trap, trapping electrons and preventing their recombination with holes. Zeolites can function as electron sinks, delaying recombination and increasing the lifespan of reactive charge carriers, which improves photocatalytic activity.

• Charge carrier separation: the interaction between TiO_2 and CP allows for charge carrier separation. The CP structure can take electrons from TiO_2, while the nanoparticles can deliver holes, minimizing recombination and enhancing photocatalytic performance. Zeolite-supported TiO_2 composites promote the generation of reactive species like hydroxyl radicals ($^{\bullet}OH$), which are necessary for the breakdown of organic contaminants.

• Better light absorption: particularly in the UV-Vis region, the unique structure of the CP can improve light absorption because of its high surface area and pore volume, which can scatter light in a way that lengthens the optical path within the composite. This scattering effect can increase the absorption of light by TiO_2 nanoparticles, which can increase the generation of electron–hole pairs and improve photocatalytic activity.[27]

• Fe^0 acts as a new conduction band, lies below the conduction band of TiO_2 and reduces the bandgap difference of TiO_2, which previously worked efficiently only under UV radiation. The electron present in the valence band of TiO_2 can now easily jump to the new conduction band, *i.e.* Fe^0, under solar radiation, as shown Fig. 5.[28]

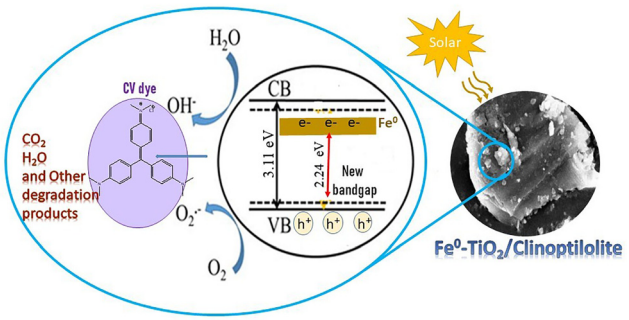

Fig. 5 Reduction in the bandgap of TiO_2/CP by Fe^0 doping on TiO_2/CP.

3.7. Application of TiO_2/CP photocatalyst

a. Removal of CV dye from aqueous medium *via* adsorption and photocatalytic degradation. In a heterogeneous photocatalysis, the first process is adsorption, which takes place in the dark, and then, the degradation process starts upon exposure of the solution containing dyes and photocatalyst to radiation. The percentage of dye removed from an aqueous solution is not significantly affected by adsorption alone. A substantial portion of the dye in an aqueous solution is removed using the synthesized TiO_2/CP photocatalyst through a combined effect of adsorption and photocatalytic degradation.

A calibration curve for CV dye was constructed by plotting absorbance against concentration (in ppm), revealing a linear relationship, as shown in Fig. S4 Chart A. The resulting analytical equation and correlation coefficient (R^2) were derived

and utilized for data analysis, enabling the calculation of the removal percentage and adsorption capacity:

$$y = 0.0776x - 0.0096, \quad (5)$$

$$R^2 = 0.9956. \quad (6)$$

b. Effect of the calcination temperature on the removal efficiency of the photocatalyst. Calcination significantly influences the phase, crystallinity, and properties of TiO_2, with anatase being the dominant phase at both 500 and 600 °C. At 500 °C, TiO_2 nanoparticles exhibit improved crystallinity compared to lower temperatures, but some amorphous content may remain, potentially reducing degradation efficiency. In contrast, calcination at 600 °C enhances crystallization and particle growth, resulting in higher crystallinity and larger particle sizes, as confirmed by TEM analysis. The TEM images, as shown in Fig. 2(I) and (J), reveal nearly spherical nanoparticles consistent with the anatase phase.[29–31] Anatase TiO_2, with its tetragonal structure and 3.11 eV band gap,[32,33] is particularly suitable for photocatalysis due to its stability up to 712 °C.[34] As the primary catalyst, TiO_2 plays a crucial role in the photocatalytic degradation of CV dye, leveraging its crystalline structure and properties to facilitate efficient degradation.

TiO_2-500 °C has a band gap energy of 3.30 eV.[35] This high band energy is not suitable for the degradation of CV dye under solar radiation. The TiO_2 synthesized *via* the sol–gel method was calcined at two different temperatures (500 and 600 °C). The photocatalytic performance of TiO_2 calcined at 500 and 600 °C (TiO_2-500 °C and TiO_2-600 °C) temperatures was investigated, and the results summarized in Fig. S4 Chart B revealed that TiO_2-600 °C has a high removal efficiency of CV dye compared to TiO_2-500 °C.

c. Effect of the concentration of Titania in TiO_2/CP on the removal of dye. The adsorptive and degradation photocatalytic efficiency of different as-synthesized photocatalysts were comparatively investigated. The bare anatase phase TiO_2 has low adsorption activity and needs to be combined with materials with a high surface area and adsorption capacity. The CP zeolite played a positive role, as an adsorbent, for CV dye degradation, but bare CP exhibited no degradation properties. The combined composite of TiO_2 and CP enhances the adsorption and degradation properties of each other and gives a high removal% of CV dye. Table 2 shows that among the four different molarities (0.1, 0.25, 0.5 and 1.0 M) of $TiCl_4$ in TiO_2/CP composites, 0.25 M TiO_2/CP performed the highest degradation of CV dye in aqueous solution. However, when the concentration of titania increased, it occupied the maximum surface of CP zeolite and led to a reduction in the adsorption capacity of the composite for CV dye.

d. Effect of pH on reaction media. The TiO_2/CP composites showed the highest degradation efficiency of CV dye at pH 6.[7] At first instance, the photo-catalysis process was carried out without adjusting the pH of the solution, which led to less removal of CV dye from aqueous solution. Then, the same process was repeated in duplicate, with the pH adjusted to 6 using a 1% HCl solution. The results summarized in Table S1 illustrate that all the TiO_2/CP composites give maximum removal efficiency of CV dye in the pH range of 5.5–6.5.

Table 2 Removal% and adsorption capacity of CV dye using different photocatalysts

S. no	Photocatalyst/ sample	Radiation source	Removal%	Adsorption capacity
1	CP	UV	51.19	13.82
2	TiO_2-500 °C	UV	39.29	20.22
3	TiO_2-600 °C	UV	58.67	24.13
4	TiO_2-600 °C	Solar	48.45	10.47
5	0.1 M TiO_2/CP	UV	90.00	21.51
6	0.25 TiO_2/CP	UV	92.36	22.08
7	0.5 TiO_2/CP	UV	88.06	21.05
8	1.0 TiO_2/CP	UV	81.87	19.57
9	0.1 TiO_2/CP	Solar	88.52	21.16
10	0.25 TiO_2/CP	Solar	84.24	20.14
11	0.5 TiO_2/CP	Solar	86.99	20.79
12	1.0 TiO_2/CP	Solar	71.40	17.07
13	Fe^0–TiO_2/CP	Solar	77.89	17.91
14	Fe^0–TiO_2/CP	UV	80.19	12.38
15	Fe^0–TiO_2	Solar	76.01	16.37
16	Fe^0–TiO_2	UV	84.77	16.89

e. Effect of time interval of reaction. As shown in Fig. 6(A), the pure parent CP gives total adsorption of 13.8% and total removal of 51% in 120 minutes. The bar of TiO_2 (Fig. 6(A) and (B)) gives the maximum 58 and 48% removal of CV dye in 120 minutes under UV and solar radiations, respectively. The 0.25 M TiO_2/CP composite, as depicted in Fig. 6(A), performed the highest removal efficiency of about 92.3% in 120 minutes under UV radiation. Additionally, 0.1 M TiO_2/CP, as shown in Fig. 6(B), revealed the highest CV dye removal of 88.5% under solar radiation in 120 minutes.

The UV-vis spectra of CV dye degradation using various photocatalysts show a decrease in absorbance over time, indicating a reduction in dye concentration (Fig. 6(C) and (D) and Fig. S5).

As irradiation time increases, the characteristic peak's absorbance decreases, and the peak shifts downward, signifying enhanced removal efficiency. After 120 minutes, the peaks nearly flatten, suggesting that optimal removal is achieved within this timeframe.

f. Effect of the type of radiation on degradation. The percentage degradation rates of TiO_2, CP, and various molar composites of TiO_2-CP were investigated under two sources, such as UV and solar irradiation. Table 2 shows the removal efficiencies and adsorption capacities. The results demonstrate that the degradation of CV dye under a UV source is much faster than solar, as shown in Fig. S4 Chart C, and TiO_2 exhibits minimal activity in the presence of visible light compared to UV rays, which is found in close agreement with the literature.[36] This occurs due to the TiO_2's broad band gap, which limits its potential but can be increased through surface modification techniques.

In order to improve TiO_2 efficiency under solar radiation, the strategy used was to synthesize the Fe^0–TiO_2/CP composite. The co-doping of Fe^0 with TiO_2 reduces the band gap of TiO_2, allowing it to operate efficiently under solar radiation. The degradation efficiency of Fe^0–TiO_2/CP composite under solar

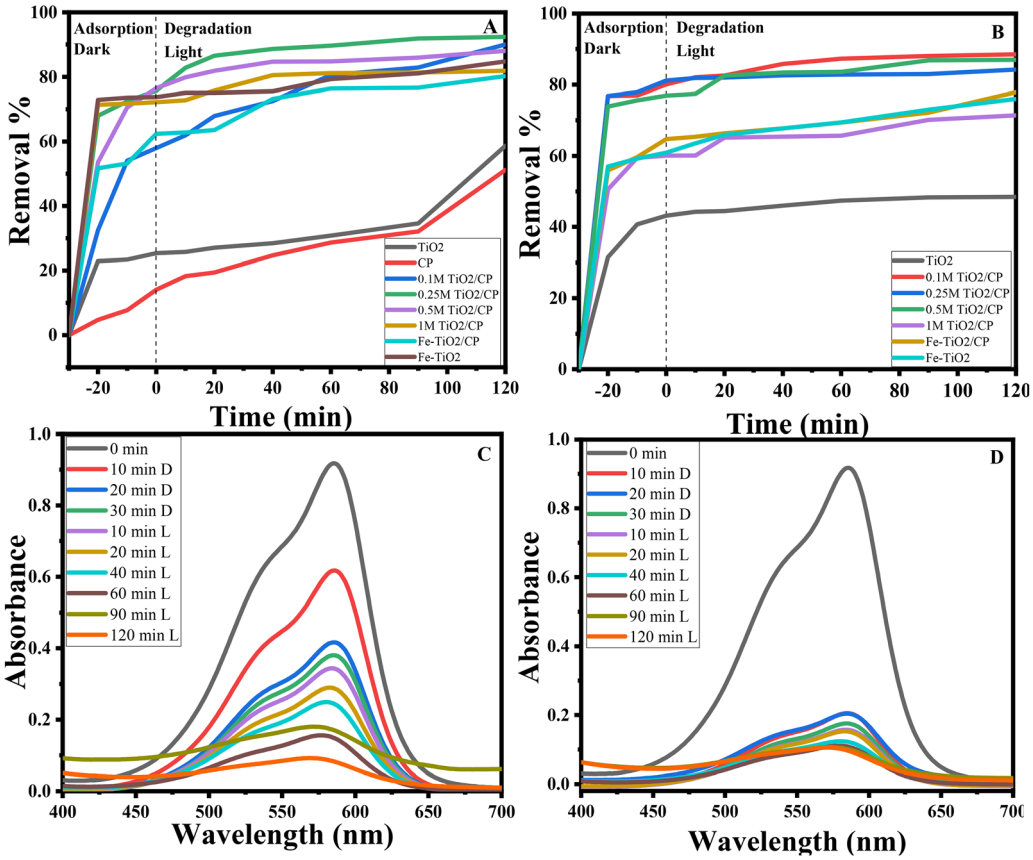

Fig. 6 Removal percent *vs.* time in UV (A) and solar radiations (B). UV-Visible spectra of CV dye in UV (C) and solar radiations (D) D = dark and L = light.

radiation was not enhanced after doping with Fe^0. As shown in Table 2, the maximum degradation of Fe^0–TiO_2/CP composite is 77.8%, which is less than 0.1 M TiO_2/CP with 88.5% removal of CV dye under solar radiation in 120 minutes. However, the degradation efficiency of bare TiO_2 from TiO_2-600 °C (48%) to Fe^0–TiO_2 (76%) under solar radiation is increased, as shown in Table 2. The Fe^0 doping did not considerably increase the degradation efficiency of TiO_2/CP, which is confirmed by the XRD patterns, SEM images, TG/DTG analysis and BET analysis. As the zerovalent iron particles do exist in chain like structure, which have a sponge-like morphology and cover the external surface area of the composite, it results in a decreased average pore size of the Fe^0–TiO_2/CP, as shown in Table 1. The BET analysis showed that the average pore size of 0.1 MTiO_2/CP (23.1 nm) decreased in the Fe^0–TiO_2/CP (13.9 nm) composite, leading to less adsorption of CV dye. This was also confirmed by the results reported in Table 2, which showed that 0.1 M TiO_2/CP composite showed 21 and 21.5 mg g^{-1} of maximum adsorption capacity under UV and solar radiations, respectively, while the same composite with Fe0 doped (Fe^0–TiO_2/CP) offered maximum adsorption capacities of 17 and 12 mg g^{-1} under UV and solar radiations, respectively.

3.8. Kinetic study of adsorption and photocatalytic degradation of CV dye

The adsorption process of CV dye on the surface of the photocatalyst is dependent on both the amount of CV dye in aqueous solution and the available active sites on titania-supported clinoptilolite composites. Adsorption kinetics studies were carried out using pseudo-first order (PFO) and pseudo-second order (PSO) models. The adsorption process of CV dye was found to follow the PSO model, which explains why adsorption is a two-site occupancy. The following two equations are applied to the adsorption process:

$$\ln(q_e - q_t) = \ln q_e - k_1 t, \quad (7)$$

$$\frac{t}{q_t} = \frac{1}{k_2 \cdot q_e^2} + \frac{t}{q_e}, \quad (8)$$

where q_e and q_t are the adsorbed amount of dye at equilibrium and time t, respectively, and k_1 and k_2 are the PFO and PSO constants, respectively.[7]

For PSO, the R^2 values are higher than those for PFO, as shown in Table 3. The adsorption of CV dye on all TiO_2/CP composites showed the best fit to PSO. As depicted in Fig. 7(A) and (B), the experimental curve is a straight line plotted with PSO and PFO, respectively, for the adsorption of CV dye on a 0.1 M TiO_2/CP composite. R^2 values for PSO is 0.9685 and for PFO is 0.6973, confirming that the adsorption process best fits the PSO kinetic model.

The degradation process follows the PFO model, in which the reaction depends on the initial concentration of the dye in the solution. In the process of CV dye degradation, $^{\bullet}OH$ and

Table 3 Kinetics study of the adsorption and degradation of CV dye

S. no	Photocatalyst/sample	Radiation source used	$q_e$exp	Adsorption						Degradation	
				Pseudo 1st order			Pseudo 2nd order			Pseudo 1st order	
				$q_e$calc	k_1	R^2	$q_e$calc	k_2	R^2	K	R^2
1	CP	UV	3.81	5.37	0.06	0.88	6.04	0.02	0.69	—	—
3	TiO_2-600 °C	UV	10.43	5.03	0.07	0.59	10.36	0.16	0.99	0.004	0.77
4	TiO_2-600 °C	Solar	9.32	6.48	0.08	0.73	9.57	0.06	0.99	0.0009	0.92
5	0.1 M TiO_2/CP	UV	19.86	9.13	0.10	0.69	16.98	0.03	0.99	0.011	0.98
6	0.25 TiO_2/CP	UV	20.44	8.10	0.09	0.62	19.19	0.13	0.99	0.008	0.86
7	0.5 TiO_2/CP	UV	19.99	11.30	0.09	0.80	19.38	0.04	0.99	0.005	0.89
8	1.0 TiO_2/CP	UV	14.08	6.06	0.09	0.53	15.95	0.04	0.98	0.003	0.80
9	0.1 TiO_2/CP	Solar	19.13	5.45	0.08	0.42	19.19	0.30	0.99	0.005	0.89
10	0.25 TiO_2/CP	Solar	19.39	11.05	0.09	0.81	19.05	0.04	0.99	0.001	0.92
11	0.5 TiO_2/CP	Solar	18.39	9.09	0.09	0.69	18.45	0.05	0.99	0.005	0.87
12	1.0 TiO_2/CP	Solar	14.54	7.45	0.09	0.62	14.59	0.09	0.99	0.001	0.94
13	Fe^0–TiO_2/CP	Solar	13.17	5.71	0.08	0.55	13.97	0.15	0.99	0.004	0.93
14	Fe^0–TiO_2/CP	UV	9.63	6.17	0.07	0.78	9.49	0.09	0.98	0.006	0.91

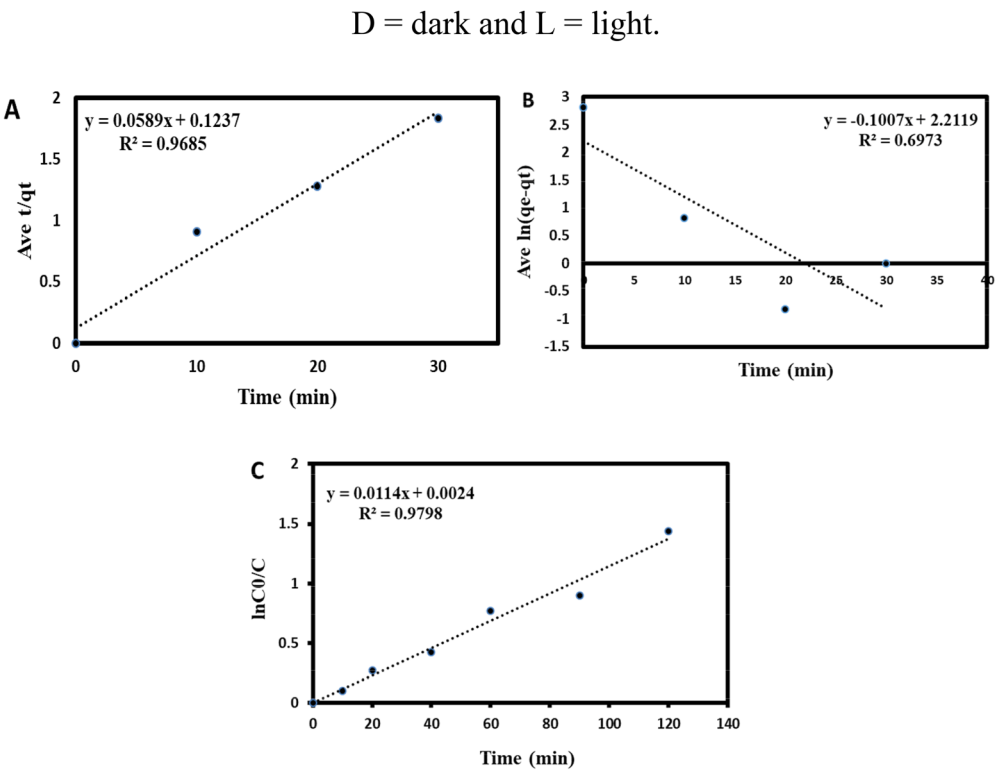

Fig. 7 (A) Adsorption study of CV dye using pseudo-second-order model and (B) pseudo-first-order model, and degradation kinetics of CV dye using (C) pseudo-first-order model.

$O_2^{\bullet-}$ are continuously generated by UV and solar radiations falling on the photo-catalyst containing semiconductor TiO_2. These radicals are in excess, and the reaction rate depends merely on the dye concentration. The following equation is applied for degradation:

$$\ln\left(\frac{C_0}{C}\right) = k \cdot t, \tag{9}$$

where C_0 and C are the concentrations of dye at time 0 and time t, respectively, k is the rate constant and t is the interval time.[7]

3.9. Scavenger study using EDTA, IPA and *p*-BQ

The photocatalytic mechanisms of TiO_2/CP and Fe^0–TiO_2/CP composites were investigated through free radical scavenger experiments to identify the key active species involved in the degradation of CV dye. In each experiment, 10 mL of 0.1 M solutions of specific scavengers, including isopropyl alcohol (IPA) to capture hydroxyl radicals ($^{\bullet}OH$), ethylenediamine tetra-acetic acid (EDTA) to capture holes (h^+), and benzoquinone (BQ) to capture superoxide radicals ($^{\bullet}O_2^-$), was added to the CV dye solution before photodegradation.[37] The results showed that the addition of BQ moderately reduced the degradation of

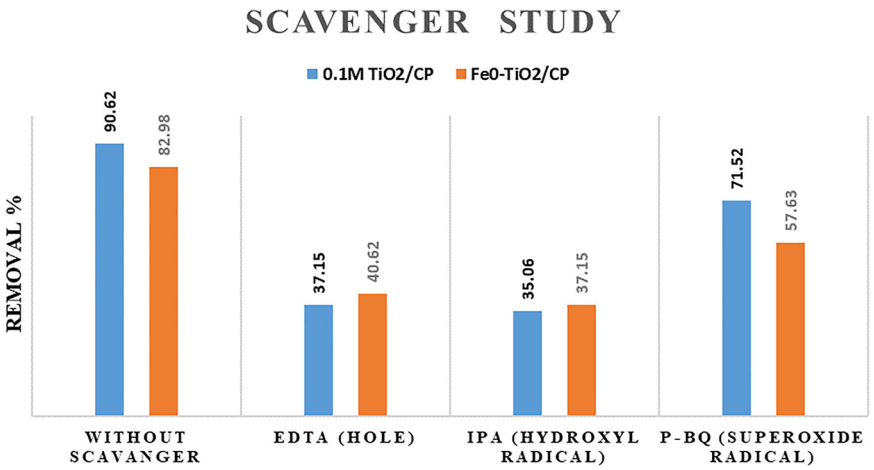

Fig. 8 Scavenger study using EDTA, IPA and *p*-BQ.

CV dye, indicating that $^{\bullet}O_2^-$ plays an important role in both reaction systems. In contrast, the addition of EDTA and IPA significantly reduced the degradation rate of CV dye, by 37 and 40% for EDTA and by 35 and 37% for IPA in the TiO_2/CP and Fe^0–TiO_2/CP systems, respectively. This suggests that holes and $^{\bullet}OH$ are crucial for the photocatalytic process. Overall, Fig. 8 illustrates that h^+, $^{\bullet}OH$, and $^{\bullet}O_2^-$ are the main active radicals responsible for the degradation of CV dye in both photocatalytic systems.

The migration direction of photogenerated charge carriers in a composite is closely related to the band edge positions of the semiconductors. To determine these positions, the following formulas are used:

$$E_{CB} = X - E_C - 0.5\,E_g \quad (10)$$

for the conduction band (E_{CB}) edge potential,

$$E_{VB} = E_{CB} + E_g \quad (11)$$

for the valence band (E_{VB}) edge potential.

Here, X represents the absolute electronegativity of the semiconductor (5.81 eV), and E_C is the energy of free electrons on the hydrogen scale, which is 4.50 eV. Using these formulas, the calculated edge potentials for TiO_2/CP are 2.8 eV for the valence band (E_{VB}) and −0.18 eV for the conduction band (E_{CB}).[37,38]

a. Photocatalytic mechanism of TiO_2/CP. According to the traditional photocatalytic degradation mechanism, when TiO_2 in the TiO_2/CP composite is exposed to light irradiation, it generates photoelectrons that jump from the valence band (VB) to the conduction band (CB). The holes (h^+) in the VB of TiO_2, with an edge potential of 2.8 eV, can react with H_2O through an oxidation process to produce hydroxyl radicals ($^{\bullet}OH$), given that the VB edge potential is more positive than the H_2O/OH potential (2.40 eV *vs.* NHE).[38] However, the electrons in the CB of TiO_2, with an edge potential of −0.18 eV, are not sufficiently negative to reduce O_2 and form superoxide radicals ($^{\bullet}O_2^-$) since the CB edge potential is more positive than the O_2/$^{\bullet}O_2^-$ potential (−0.046 eV *vs.* NHE).[2] As a result, the TiO_2/CP photocatalyst does not produce a significant amount of $^{\bullet}O_2^-$ to oxidize CV dye, which is consistent with the findings from the free radical scavenger experiments. This analysis supports the proposed photocatalytic mechanism for the TiO_2/CP composite.

b. Photocatalytic mechanism of Fe^0–TiO_2/CP. The XRD pattern of the used Fe^0–TiO_2/CP sample, as shown in Fig. 1(B)-(g), clearly exhibits a peak corresponding to Fe^0 at a 2θ degree of 44°. This confirms the presence of Fe^0 in the composite. According to the proposed mechanism illustrated in Fig. 5, when TiO_2 is irradiated, it generates photoelectrons (e^-) and holes (h^+). The electrons in the conduction band of TiO_2 are then transferred to Fe^0, which acts as an electronic medium. This electron transfer is facilitated by the electron trap constructed by Fe^0, allowing for the spatial isolation of photogenerated electron–hole pairs. As a result, the undesirable recombination of electrons and holes is greatly limited, enhancing the photocatalytic efficiency of the Fe^0–TiO_2/CP composite.

In the Fe^0–TiO_2/CP composite, the electrons associated with Fe^0, which have a reduction potential of approximately −0.41 to −0.44 V,[39,40] can combine with oxygen in water to form superoxide radicals ($^{\bullet}O_2^-$). The potential for forming superoxide radicals is −0.046 eV *vs.* NHE, and these radicals can mineralize CV dye. Simultaneously, the holes in the valence band of TiO_2, with an edge potential of 2.8 eV, can directly react with CV dye to mineralize it. Furthermore, the holes in the TiO_2 valence band can react with water to form hydroxyl radicals ($^{\bullet}OH$) due to the valence band potential being higher than the H_2O/$^{\bullet}OH$ potential (2.40 eV *vs.* NHE). These hydroxyl radicals can then oxidize CV dye into degradation products. This proposed mechanism is consistent with the results of free radical scavenger experiments, which identify the reactive species involved in the photocatalytic degradation process using the Fe^0–TiO_2/CP composite.

The formation of superoxide radical anions ($^{\bullet}O_2^-$) occurs when electrons in the CB of TiO_2 or Fe^0 combine with oxygen through a reduction process. A key reason why the Fe^0–TiO_2/CP system produces more superoxide radicals than the TiO_2/CP

system lies in the difference in their reduction potentials. Specifically, the conduction band potential of TiO_2 (−0.18 eV) is not sufficiently negative to reduce oxygen molecules to form superoxide radicals, given that the $O_2/^{\bullet}O_2^-$ potential is −0.046 eV *vs.* NHE. In contrast, the reduction potential of Fe^0 (−0.41 to −0.44 V)[39,40] is more negative than the $O_2/^{\bullet}O_2^-$ potential, allowing it to easily reduce oxygen molecules and produce superoxide radicals. The redox potentials of the conduction band and valence band of TiO_2/CP are −0.18 and 2.8 eV, respectively, indicating that TiO_2/CP acts as a mild reducing and strong oxidizing photocatalyst.[41]

3.10. Degradation pathway and identification of intermediates using H-ESI-MS analysis

The various intermediates formed during the mineralization of CV dye by Fe^0–TiO_2/CP and 0.1 M TiO_2/CP photocatalysis are shown in Fig. S6. The reaction intermediates were examined using the H-ESI-MS technique. The results of the obtained H-ESI mass spectra are summarized in Table 4, and the mechanism is shown in Fig. 9, Scheme 1. Nineteen intermediates were identified.

Route 1: the attack of radical species on the CV dye molecule is a crucial step in the *N*-de-methylation pathway. This process begins with a radical species, such as $^{\bullet}OH$, abstracting a hydrogen atom from a methyl substituent of the amino group, which forms a carbon-centered radical. Depending on the specific reaction conditions, other radical species such as superoxide ($O_2^{\bullet-}$) radicals may also be involved in the attack on the dimethylamine group. This carbon-centered radical is highly reactive and can undergo further reactions. Another radical species then attacks the dimethylamine group, leading to the formation of a mono-de-methylated intermediate.

After the second radical attack, the intermediate molecule remains positively charged due to the delocalized positive charge over the conjugated triphenylmethane system of the original CV molecule. Although a neutral methyl group is removed during demethylation, the positive charge persists albeit with a slightly altered distribution. This positively charged intermediate can still be adsorbed on the photocatalyst surface, where further stepwise demethylation occurs.[42]

The cleavage of the C–N bond during the second radical attack is a heterolytic process. The first attack involves homolytic cleavage, in which a radical abstracts a hydrogen atom from a methyl group, leaving a carbon-centered radical intermediate. The second radical species then interacts with this intermediate, triggering a rearrangement in which the C–N bond is broken unevenly.

The nitrogen atom retains both electrons from the bond, while the carbon-centered radical remains a smaller neutral molecule, such as formaldehyde. This heterolytic cleavage results in a final, less-methylated cationic intermediate and a neutral byproduct, with the positive charge remaining on the larger triphenylmethane structure.[43]

The *N*-de-methylated intermediates of CV were identified using H-ESI mass spectrometry. The molecular ion peaks, as shown in Fig. S6 and listed in Table 4, confirmed the presence of various intermediates. These species correspond to three pairs of isomeric molecules with two to four fewer methyl groups than CV. For instance, **B** is formed by the removal of a methyl group from the CV molecule. In the first pair of isomers, **C** is formed by the removal of two methyl groups from two sides of the CV molecule, while D is produced by the removal of two methyl groups from the same side of the CV structure.

In the second pair of isomers, **E** is formed by the removal of three methyl groups from each side of the CV molecule, while **F** is produced by the removal of two methyl groups from one side and one methyl group from the other side. In the third pair of isomers, **H** is formed by the removal of two methyl groups from two sides of the CV molecule, while **G** is produced by the removal of two methyl groups from the same side and one methyl group from the remaining two sides. Further, *N*-de-methylation leads to the formation of **I** and **J**. The *N*-de-methylated intermediates (**A–J**) are shown in Fig. 9, Scheme 1

Table 4 Degradation intermediates of CV dye

H-ESI-MS peaks	Intermediates	ESI-MS spectrum ions (*m*/*z*)
A	*N*,*N*,*N*′,*N*′,*N*″,*N*″-Hexamethylpararosaniline CV	372.42
B	*N*,*N*-Dimethyl-*N*′,*N*′-dimethyl-*N*″-methylpararosaniline	358.50
C	*N*,*N*-Dimethyl-*N*′-methyl-*N*″-methylpararosaniline	344.67
D	*N*,*N*-Dimethyl-*N*′,*N*′-methylpararosaniline	344.33
E	*N*-Methyl-*N*′-methyl-*N*″-methylpararosaniline	332.83
F	*N*,*N*-Dimethyl-*N*′-methylpararosaniline	330.67
G	*N*-Methyl-*N*′-methylpararosaniline	316.75
H	*N*,*N*-Dimethylpararosaniline	316.50
I	*N*-Methylpararosaniline	302.25
J	Pararosaniline	288.83
K	4-(*N*,*N*-dimethylamino)phenol	138.08
L	4-(*N*,*N*-Dimethylamino)-4-(*N*,*N*-dimethylamino)benzophenone	269.92
M	4-(*N*-Methylamino)phenol	124.08
N	4-aminophenol	110.83
O	4-(*N*,*N*-Dimethylamino)-4-(*N*-methylamino)benzophenone	255.00
P	4-(*N*,*N*-Dimethylamino)-4-aminobenzophenone	240.75
Q	4-(*N*-Methylamino)-4-(*N*-methylamino)benzophenone	240.67
R	4-(*N*-Methylamino)-4-aminobenzophenone	226.00
S	4,4-Bis-aminobenzophenone	213.83

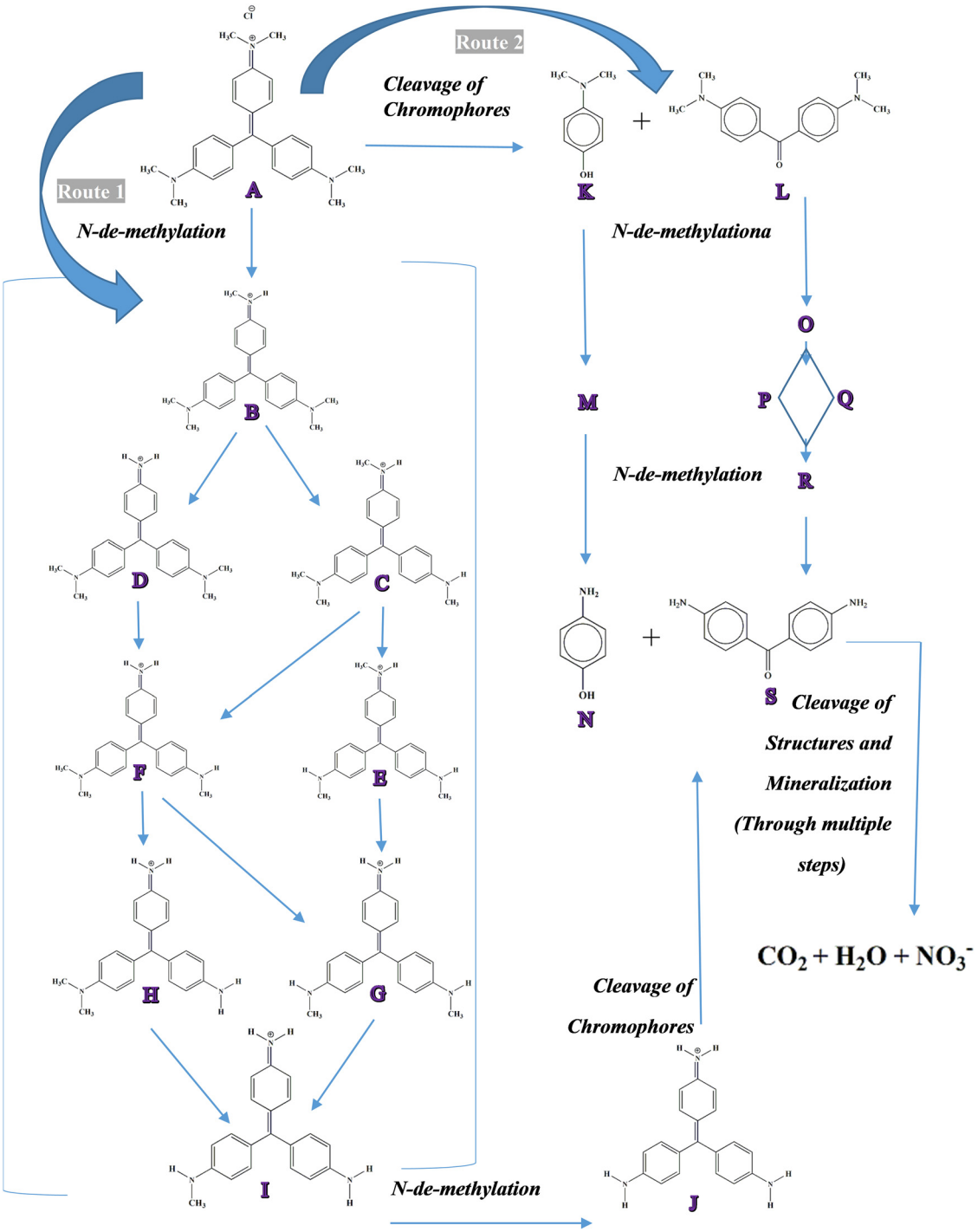

Fig. 9 Scheme 1: Degradation pathways of CV dye.

(Route 1). After that, the direct attack of the (•OH) radical on the central carbon of **J** produces **N** and **S** through chromophore cleavage.[44]

Route 2: however, the degradation of CV is initiated by the highly reactive hydroxyl radical (•OH), which attacks the central carbon atom of the molecule. This central carbon is part of the extensively conjugated triphenylmethane chromophore responsible for CV's deep purple color. The attack likely occurs due to the electrophilic nature of the central carbon, making it susceptible to nucleophilic species like the hydroxyl radical or radical attack, leading to bond breaking. The hydroxyl radical's attack initiates the cleavage of a carbon–carbon bond connecting one of the *N*,*N*-dimethylaminophenyl rings to the central carbon atom, directly breaking the extended conjugation system of the CV molecule. This bond breaking results in the formation of intermediates, including 4-(dimethylamino)

phenol (**K**), which is formed from the cleavage of one of the *N*,*N*-dimethylaminophenyl groups. Another intermediate, 4-(*N*,*N* dimethylamino)-4-(*N*,*N*-dimethylamino)benzo-phenone (**L**), also known as Michler's ketone, is formed from the remaining two *N*,*N*-dimethylaminophenyl groups still attached to the central carbon, which is now part of a ketone structure after bond rearrangement and oxygen incorporation. Afterwards, compounds **N** and **S** were possibly formed by a series of *N*-de-methylated intermediates in a stepwise manner from **K** and **L**, respectively, as shown in Fig. 9, Scheme 1 (Route 2). The degradation process does not necessarily stop at these intermediates. They can undergo further reactions, such as *N*-demethylation, ring-opening, and eventual mineralization to simpler, less toxic compounds, like CO_2 and H_2O, or other intermediates, like carboxylic acids, depending on the specific reaction conditions and the presence of other oxidizing agents.[45,46]

4. Conclusion

In order to enhance the removal efficiency of CP as support and synthetic TiO_2, the TiO_2/CP, Fe^0–TiO_2 and Fe^0–TiO_2/CP composites were successfully synthesized *via* sol–gel and borohydride reduction methods. The characteristic peaks of CP at 2θ = 9.8°, 22.1°, 26.4°, 30.1°, and 35.7° revealed that the CP crystalline structure remained intact in TiO_2/CP after TiO_2 doping. The sheet-like/multi-layers/plate-like morphology of CP was unaffected under a high calcination temperature of 600 °C, confirming that it is thermally stable in all TiO_2/CP composites. The SEM and BET results showed that Fe^0 particles with a spherical shape and spongy nature covered the maximum surface area of CP zeolite after doping on TiO_2/CP composites. Furthermore, the Fe^0 doping reduces the adsorption capacity and removal efficiency in Fe^0–TiO_2/CP composite by reducing the composite's average mesopore size from TiO_2/CP (23.1 nm) to Fe^0–TiO_2/CP (13.9 nm), and this decreased efficiency is also reconfirmed by the decreased peak intensities of Fe^0–TiO_2/CP composite's in XRD patterns.

According to TG/DTG profiles, the CP, TiO_2 and their composites showed thermal stability at higher temperatures up to 900 °C. Dehydration of water caused a very minor loss of weight, but no additional structural or internal changes were noticed. The TiO_2 removed the maximum amount of CV dye (58 and 48%) under UV and solar irradiations. In addition, a maximum 92% removal of CV dye was achieved by 0.25 MTiO_2/CP composite under UV radiation compared to solar radiation, whereas a maximum CV dye removal of 88% was achieved by 0.1 M TiO_2/CP under solar radiation. Furthermore, the band gap of 0.1 M TiO_2/CP was significantly reduced, which in turn showed higher removal efficiency in solar radiations.

Scavenger study showed that the TiO_2/CP composite primarily generates $^{\bullet}OH$ radicals in CV dye degradation, while the Fe^0–TiO_2/CP composite produces both $^{\bullet}OH$ and $^{\bullet}O_2^-$ radicals, which have played a vital role in enhancing photocatalytic efficiency due to the favorable reduction potential of Fe^0. The degradation ability of Fe^0–TiO_2/CP composites to produce $^{\bullet}O_2^-$ radicals significantly contributes to enhancing their efficiency.

The degradation of CV occurs through two routes: route 1 involves stepwise *N*-de-methylation *via* radical attacks, breaking C–N bonds and forming less-methylated intermediates, while Route 2 involves hydroxyl radical attack on the central carbon, cleaving C–C bonds and disrupting the conjugated chromophore structure. Both routes lead to the breakdown of the CV dye molecule. In conclusion, using CP as a support material for TiO_2 is a significant option because CP is neutral, abundant in nature, and inexpensive, making TiO_2/CP composites an eco-friendly photocatalyst that offers a promising solution for the removal of CV dye.

Author contributions

Nazia Aziz: writing – original draft, investigation, methodology, validation, visualization, data curation, formal analysis. Hamida Panezai: writing – review & editing, visualization, supervision, project administration, conceptualization, resources. Jihong Sun: validation, resources. Noor Samad Shah: Validation, resources. Raza Ullah: data analysis, validation. Ruohan Xu: Resources. Zakira Jogezai: formal analysis.

Conflicts of interest

There are no conflicts to declare.

Data availability

The data supporting this article are summarized in this manuscript and are included in the Supplementary information (SI). Supplementary information is available. See DOI: **https://doi.org/10.1039/d5ma00658a**.

Raw data are available upon request from the corresponding author.

Acknowledgements

This study was financially supported by the Higher Education Commission (HEC) of Pakistan under HEC-NRPU research project no. 16884, and Miss. Nazia Aziz acknowledges the Higher Education Commission for HEC-NRPU Research Assistantship. VSK ProZeo zeolite is gratefully acknowledged for providing Clinoptilolite zeolite.

Notes and references

1 A. Juarez, Ensure availability and sustainable management of water and sanitation for all, *Mining, Materials, and the Sustainable Development Goals*, 2020, pp. 51–60.
2 P. Chowdhary, R. N. Bharagava, S. Mishra and N. Khan, Role of industries in water scarcity and its adverse effects on

environment and human health, *Environmental concerns and sustainable development*, 2019, pp. 235–256.
3 C. O. Aniagor and M. C. Menkiti, Synthesis, modification and use of lignified bamboo isolate for the renovation of crystal violet dye effluent, Applied Water, *Science*, 2019, **9**, 77.
4 M. S. Khan, M. Khalid and M. Shahid, What triggers dye adsorption by metal organic frameworks? The current perspectives, *Mater. Adv.*, 2020, **1**, 1575–1601.
5 R. Ullah, J. Sun, A. Gul and S. Bai, One-step hydrothermal synthesis of TiO_2-supported clinoptilolite: An integrated photocatalytic adsorbent for removal of crystal violet dye from aqueous media, *J. Environ. Chem. Eng.*, 2020, **8**, 103852.
6 R. Ullah, C. Liu, H. Panezai, A. Gul, J. Sun and X. Wu, Controlled crystal phase and particle size of loaded-TiO_2 using clinoptilolite as support via hydrothermal method for degradation of crystal violet dye in aqueous solution, *Arabian J. Chem.*, 2020, **13**, 4092–4101.
7 R. Ullah, J. Sun, A. Gul, T. Munir and X. Wu, Evaluations of physico-chemical properties of TiO_2/clinoptilolite synthesized via three methods on photocatalytic degradation of crystal violet, *Chin. J. Chem. Eng.*, 2021, **33**, 181–189.
8 S. B. Khan, M. Hou, S. Shuang and Z. Zhang, Morphological influence of TiO_2 nanostructures (nanozigzag, nanohelics and nanorod) on photocatalytic degradation of organic dyes, *Appl. Surf. Sci.*, 2017, **400**, 184–193.
9 A. S. M. Nur, M. Sultana, A. Mondal, S. Islam, F. N. Robel, A. Islam and M. S. A. Sumi, A review on the development of elemental and codoped TiO_2 photocatalysts for enhanced dye degradation under UV–vis irradiation, *J. Water Process Eng.*, 2022, **47**, 102728.
10 K. H. Rahman and A. K. Kar, Influence of catalyst loading on photocatalytic degradation efficiency of CTAB-assisted TiO_2 photocatalyst towards methylene blue dye solution, *Bull. Mater. Sci.*, 2022, **45**, 18.
11 X. Duan, J. Yang, G. Hu, C. Yang, Y. Chen, Q. Liu, S. Ren and J. Li, Optimization of TiO2/ZSM-5 photocatalysts: Energy band engineering by solid state diffusion method with calcination, *J. Environ. Chem. Eng.*, 2021, **9**, 105563.
12 M. M. Khan, S. A. Ansari, D. Pradhan, M. O. Ansari, D. H. Han, J. Lee and M. H. Cho, Band gap engineered TiO_2 nanoparticles for visible light induced photoelectrochemical and photocatalytic studies, *J. Mater. Chem. A*, 2014, **2**, 637–644.
13 E. Polat, M. Karaca, H. Demir and A. N. Onus, Use of natural zeolite (clinoptilolite) in agriculture, *J. Fruit Ornamental Plant Res.*, 2004, **12**, 183–189.
14 E. G. Richard, The science and (lost) art of psoralen plus UVA phototherapy, *Dermatol. Clin.*, 2020, **38**, 11–23.
15 D. I. Anwar and D. Mulyadi, Synthesis of Fe–TiO_2 composite as a photocatalyst for degradation of methylene blue, *Procedia Chem.*, 2015, **17**, 49–54.
16 J. D. Clogston and A. K. Patri, Importance of physicochemical characterization prior to immunological studies, *Handbook of Immunological properties of engineered nanomaterials*., 2013, pp. 25–52.
17 N. Bibi, M. Sayed, N. S. Shah, F. Rehman, A. Naeem, T. Mahmood, S. Hussain, J. Iqbal, I. Gul, S. Gul and M. Bushra, Development of zerovalent iron and titania (Fe^0/TiO_2) composite for oxidative degradation of dichlorophene in aqueous solution: synergistic role of peroxymonosulfate (HSO_5^-), *Environ. Sci. Pollut. Res.*, 2022, **29**, 63041–63056.
18 S. Tasharrofi, Z. Rouzitalab, D. M. Maklavany, A. Esmaeili, M. Rabieezadeh, M. Askarieh, A. Rashidi and H. Taghdisian, Adsorption of cadmium using modified zeolite-supported nanoscale zero-valent iron composites as a reactive material for PRBs, *Sci. Total Environ.*, 2020, **736**, 139570.
19 R. Yuvakkumar, V. Elango, V. Rajendran and N. Kannan, Preparation and characterization of zero valent iron nanoparticles, *Dig. J. Nanomater. Bios.*, 2011, **6**, 1771–1776.
20 B. Alver, M. Sakizci and E. Yorukogullari, Investigation of clinoptilolite rich natural zeolites from Turkey: a combined XRF, TG/DTG, DTA and DSC study, *J. Therm. Anal. Calorim.*, 2010, **100**, 19–26.
21 R. Kukobat, R. Skrbić, P. Massiani, K. Baghdad, F. Launay, M. Sarno, C. Cirillo, A. Senatore, E. Salcin and S. G. Atlagic, Thermal and structural stability of microporous natural clinoptilolite zeolite, *Microporous Mesoporous Mater.*, 2022, **341**, 112101.
22 S. Haq, W. Rehman, M. Waseem, R. Javed and M. Shahid, Effect of heating on the structural and optical properties of TiO_2 nanoparticles: antibacterial activity, *Appl. Nanosci.*, 2018, **8**, 11–18.
23 H. Panezai, J. Sun, X. Jin and R. Ullah, Location of silver clusters confined in FAU skeleton of dehydrated bi-metallic Ag_xM_{96-x}-LSX (M = Na^+, Li^+) zeolite and resultant influences on N_2 and O_2 adsorption, *Sep. Purif. Technol.*, 2018, **197**, 418–431.
24 M. M. Viana, V. F. Soares and N. D. S. Mohallem, Synthesis and characterization of TiO_2 nanoparticles, *Ceram. Int.*, 2010, **36**, 2047–2053.
25 H. Dzinun, M. H. D. Othman and A. F. Ismail, Photocatalytic performance of TiO_2/Clinoptilolite: Comparison study in suspension and hybrid photocatalytic membrane reactor, *Chemosphere*, 2019, **228**, 241–248.
26 K. M. Alvarez, J. J. Alvarado, B. S. Soto and M. A. Hernandez, Structural and optical properties of TiO_2 and TiO_2-Zeolites composites films, *Optik*, 2018, **169**, 137.
27 S. J. Armakovic and S. Armakovic, Zeolite-Supported TiO_2 for Enhanced Photocatalytic Performance in Environmental Applications: A Review, *Catalysts*, 2025, **15**, 174.
28 E. K. Tetteh, S. Rathilal, D. Asante-Sackey and M. N. Chollom, Prospects of synthesized magnetic TiO_2-based membranes for wastewater treatment: A review, *Materials*, 2021, **14**, 3524.
29 T. A. Kandiel, L. Robben, A. Alkaim and D. Bahnemann, Brookite versus anatase TiO_2 photocatalysts: phase transformations and photocatalytic activities, *Photochem. Photobiol. Sci.*, 2013, **12**(4), 602–609.
30 B. Xue, T. Sun and J.-K. Wu, Simple Fabrication of Anatase-Brookite Mixed-Phase TiO_2 Nanoparticles with Visible-Light

Responsive Photocatalytic Activity, *Asian J. Chem.*, 2012, **24**(5), 2073.

31 S. S. El-Deen, A. M. Hashem, A. E. Abdel Ghany, S. Indris, H. Ehrenberg, A. Mauger and C. M. Julien, *et al.*, Anatase TiO_2 nanoparticles for lithium-ion batteries, *Ionics*, 2018, **24**(10), 2925–2934.

32 N. C. Horti, M. D. Kamatagi, N. R. Patil, S. K. Nataraj, M. S. Sannaikar and S. R. Inamdar, Synthesis and photoluminescence properties of titanium oxide (TiO_2) nanoparticles: Effect of calcination temperature, *Optik*, 2019, **194**, 163070.

33 Z. Wang, S. K. Saxena, V. Pischedda, H. P. Liermann and C. S. Zha, X-ray diffraction study on pressure-induced phase transformations in nanocrystalline anatase/rutile (TiO_2), *J. Phys.: Condens. Matter*, 2001, **13**, 8317.

34 K. K. Rao, S. N. Naidu and L. Iyengar, Thermal expansion of rutile and anatase, *J. Am. Ceram. Soc.*, 1970, **53**, 124–126.

35 M. Lal, P. Sharma and C. Ram, Calcination temperature effect on titanium oxide (TiO_2) nanoparticles synthesis, *Optik*, 2021, **241**, 166934.

36 M. Tanveer, G. T. Guyer and G. Abbas, Photocatalytic degradation of ibuprofen in water using TiO_2 and ZnO under artificial UV and solar irradiation, *Water Environ. Res.*, 2019, **91**, 822–829.

37 P. D. Sanadi, *et al.*, Controllable synthesis of semiconducting anatase TiO_2 nanostructures for visible light driven photocatalytic degradation of crystal violet and methylene blue dye, *Spectrochim. Acta, Part A*, 2025, 126404.

38 F. Su, P. Li, J. Huang, M. Gu, Z. Liu and Y. Xu, *et al.*, Photocatalytic degradation of organic dye and tetracycline by ternary Ag_2O/AgBr–CeO_2 photocatalyst under visible-light irradiation, *Sci. Rep.*, 2021, **11**(1), 85.

39 E. C. Lumbaque, E. R. Lopes Tiburtius, M. Barreto-Rodrigues and C. Sirtori, *et al.*, Current trends in the use of zero-valent iron (Fe^0) for degradation of pharmaceuticals present in different water matrices, *Trends Environ. Anal. Chem.*, 2019, **24**, e00069.

40 Z. Yan, J. Ouyang, B. Wu, C. Liu, H. Wang, A. Wang and Z. Li, *et al.*, Nonmetallic modified zero-valent iron for remediating halogenated organic compounds and heavy metals: A comprehensive review, *Environ. Sci. Ecotechnology*, 2024, **21**, 100417.

41 H. Adamu, Photocatalytic remediation of nitrate in aqueous environment by TiO_2-based photocatalysts—influence of organic hole scavenger on the selectivity of reaction product(s), *Online International Conference on Catalysis and Chemical Engineering*, 2021.

42 H.-J. Fan, S.-T. Huang, W.-H. Chung, J.-L. Jan, W.-Y. Lin and C.-C. Chen, *et al.*, Degradation pathways of crystal violet by Fenton and Fenton-like systems: condition optimization and intermediate separation and identification, *J. Hazard. Mater.*, 2009, **171**(1–3), 1032–1044.

43 C.-C. Chen, J. Shaya, H.-J. Fan, Y.-K. Chang, H.-T. Chi and C.-S. Lu, *et al.*, Silver vanadium oxide materials: Controlled synthesis by hydrothermal method and efficient photocatalytic degradation of atrazine and CV dye, *Sep. Purif. Technol.*, 2018, **206**, 226–238.

44 C. C. Chen, F. D. Mai, K. T. Chen, C. W. Wu and C. S. Lu, Photocatalyzed N-de-methylation and degradation of crystal violet in titania dispersions under UV irradiation, *Dyes Pigm.*, 2007, **75**(2), 434–442.

45 G. Abdolahi, D. Maryam and G. Hossein, Synthesis of starch-g-poly (acrylic acid)/ZnSe quantum dot nanocomposite hydrogel, for effective dye adsorption and photocatalytic degradation: thermodynamic and kinetic studies, *Cellulose*, 2020, **27**(11), 6467–64831.

46 B. Karan, Degradation of crystal violet dye from waters by layered MnO_2 and nanocomposite-MnO_2@ $MnFe_2O_4$ catalysts, *Hacettepe J. Biol. Chem.*, 2018, **45**, 573–580.